Nuclear Materials and Energy 37 (2023) 101534

Contents lists available at ScienceDirect

Nuclear Materials and Energy

journal homepage: www.elsevier.com/locate/nme

Spinodal decomposition and radiation damage of a FeCuMnNi high-entropy alloy

Qingwei Guo [a], Jinzhong Tian [a], Xiaotao Xu [a], Hua Hou [a,b], Peter K. Liaw [c], Yuhong Zhao [a,d,e,*]

[a] School of Materials Science and Engineering, Collaborative Innovation Center of Ministry of Education and Shanxi Province for High-performance Al/Mg Alloy Materials, North University of China, Taiyuan 030051, P R China
[b] School of Materials Science and Engineering, Taiyuan University of Science and Technology, Taiyuan 030024, P R China
[c] Department of Materials Science and Engineering, The University of Tennessee, Knoxville, Knoxville, TN, United States
[d] Beijing Advanced Innovation Center for Materials Genome Engineering, University of Science and Technology Beijing, Beijing 100083, P R China
[e] Institute of Materials Intelligent Technology, Liaoning Academy of Materials, Shenyang 110004, P R China

ARTICLE INFO

Keywords:
Multi-scale method
FeCuMnNi
High-entropy alloys
Spinodal decomposition
Radiation

ABSTRACT

The precipitation of Cu-rich phases during the irradiation process will reduce radiation resistance in Fe-Cu-Mn-Ni reactor pressure vessel steels. Therefore, high-entropy alloys with excellent radiation resistance are expected to replace reactor pressure vessel steels and become structural materials for fusion and generation IV fission reactors. This study investigated the phase formation, spinodal decomposition tendency, and radiation resistance of the FeCuMnNi high entropy alloy using a multi-scale method. The results show that FeCuMnNi alloy has a dual-phase face-centered-cubic structure. Here, for the first time, we found that the precipitation phase of the FeCuMnNi high-entropy alloy during the irradiation process is a Mn-rich phase rather than a Cu-rich phase found in conventional Fe-Cu-Mn-Ni reactor pressure vessel steels. Mn separates from the Cu-Mn-rich phase and forms Fe-Mn-Ni clusters with a Fe-Ni phase during irradiation.

Introduction

The Fe-CuMnNi alloys, categorized as a type of Reactor Pressure Vessel (RPV) steels, have been serving for a long time in the harsh environment of high temperature, high pressure, and intense irradiation. The presence of solute clusters and matrix damage (vacancies and dislocations) during irradiation in RPV steels hinders the movement of dislocations, leading to a reduction in the alloy's plasticity and causing irradiation embrittlement [1,2]. Odette et al. [3] provided an overview of the history and current status of prediction models for reactor pressure vessel (RPV) steel's ductile-to-brittle transition temperature and concluded that Cu, Ni, and P are the primary elements contributing to the embrittlement of RPV steels. Among them, Cu is the primary contributor to hardening and embrittlement in neutron-irradiated RPV steels, and it is classified as an impurity element within RPV steels [4]. Research has indicated notable differences in behavior between high-copper (>0.1 %) and low-copper (<0.1 %) RPV steels under irradiation. In high-Cu RPV steels, radiation enhanced the formation of Cu-rich phases, whereas the formation of Mn-Ni-rich phases is contingent upon the existence of Cu-rich phases [5]. Researchers have systematically examined RPV steels from various countries using Atom Probe Tomography and have consistently observed the enrichment of elements like Mn, Ni, and Si within the Cu-rich phases [6]. The presence of Cu-rich phases in RPV steels leads to increased hardness and induces irradiation hardening. In low-Cu RPV steels, the primary precipitation type induced by irradiation is the Mn-Ni-rich phase. Thermodynamic and kinetic models have confirmed that the formation of the Mn-Ni-rich phase is independent of copper [7]. Castin et al. [8] have developed a microstructure evolution theory and model that can quantitatively predict the formation of solute clusters in ferrite, confirming that the embrittlement of ferritic steel under irradiation is primarily determined by the formation of nanoscale solute clusters. Almirall et al. [9] indicated that Mn-Ni interactions play a dominant role in determining the volume fraction of Mn-Ni-Si intermetallic precipitates. The Mn-Ni-rich phase is considered one of the main factors contributing to irradiation-induced embrittlement and fracture. Consequently, the question of how to control the composition of RPV steels to enhance their radiation resistance is an urgent matter that needs to be addressed.

The high-entropy alloys (HEAs) proposed by Yeh et al. [10] and Cantor et al. [11] in 2004 have shattered the traditional concept of alloy

* Corresponding author.
E-mail address: zhaoyuhong@nuc.edu.cn (Y. Zhao).

https://doi.org/10.1016/j.nme.2023.101534
Received 15 October 2022; Received in revised form 8 October 2023; Accepted 10 October 2023
Available online 11 October 2023

design. By adjusting their composition, HEAs can exhibit a single or multi-phase structure, which possesses exceptional properties compared to traditional alloys. These properties include good corrosion and wear resistance [12], elevated-temperature thermal stability and reasonable ductility [13], high ultimate tensile strength [14], and great fatigue resistance [15]. Recent studies have indicated that some HEAs also exhibit favorable radiation resistance, such as the NiCoCrFe [16], CoCrFeMnNi [17], AlCoCrFeNi [18], and so on. Xu et al. [19] predicted the possible formation of vacancy clusters in the CoCrFeMnNi HEA based on first principles when high-energy ion or neutron irradiation causes cascade damage. The complex composition of the Ni-Co-Cr-Fe HEA restricts defect migration and alters the energy distribution, influencing defect dynamics and promoting the annihilation of radiation damage [16,19–22]. These mechanisms ultimately contribute to improved radiation tolerance in HEAs. Therefore, HEAs are considered promising structural materials for Gen-IV fission reactors [23]. However, existing research has primarily focused on single-phase HEAs, and it remains uncertain whether they can retain excellent radiation resistance when the phase structure of the HEA transitions to a dual-phase face-centered-cubic (FCC) or body-centered-cubic (BCC) solid solution. So far, there has been a lack of comprehensive investigations into the radiation resistance mechanisms of multiphase HEAs. This situation provides the motivation for this research.

The phase formation and phase decomposition trends of alloys can be accurately predicted based on the first-principles method by calculating the energy of the alloys [24]. Moreover, the calculation of alloy properties can assist in the experimental screening of high-performance alloys. From the perspective of Newtonian mechanics, molecular dynamics can predict the structural evolution of alloys by solving the interaction potential and equation of motion between atoms and studying the mechanical properties, thermodynamic properties, and anti-radiation properties of alloys [25]. This work employs a multiscale approach (experimental, first-principles, and molecular dynamics) to investigate the phase formation, decomposition tendencies, and radiation resistance properties of FeCuMnNi HEA. The phase formation of FeCuMnNi HEA was studied through experimental investigations. Furthermore, by combining first-principles calculations, the underlying reasons for the occurrence of spinodal decomposition in FeCuMnNi HEA were elucidated. The irradiation resistance of FeCuMnNi HEA was investigated via molecular dynamics simulations, providing insights into the formation mechanisms of point defects, defect clusters, and dislocation loops. To ensure comparability of results, this study employs commonly used pure Ni as reference material in contrast to FeCuMnNi HEA. This choice is made because RPV steel has a different crystal structure (BCC) compared to FeCuMnNi HEA.

Methodology

In this study, we investigated the phase formation of FeCuMnNi HEA through experiments. From these results, the FeCuMnNi HEA models were constructed using the first-principles method, and the theoretical X-ray diffraction patterns were calculated to check the model's accuracy. We analyzed the reasons behind the spinodal decomposition of FeCuMnNi HEA by calculating its formation energy, spinodal decomposition energy, and density of states (DOS). Afterward, molecular dynamics models were created to compare the radiation resistance performance of FeCuMnNi HEA with Ni.

Experiment

Metal particles of Fe, Cu, Mn, and Ni with a purity of more than 99.99 wt% (wt.%) were selected as raw materials and weighed at the nominal composition ratio of 1:1:1:1. The FeCuMnNi HEA was synthesized by arc melting under a high-purity argon atmosphere. The crystal structure of the FeCuMnNi HEA was characterized using X-ray diffraction (XRD) with CuKα radiation (RIGAKU D/Max-RB), scanning angles ranging from 20° to 90°. The microstructures in different states were characterized by Hitachi SU5000 scanning electron microscopy (SEM), and the chemical compositions in different regions were investigated using X-ray energy dispersive spectrometry (EDS) attached to SEM.

First-principles calculations

First-principles calculations were performed using the Reflex Powder Diffraction module [26] and Cambridge Sequential Total Energy Package (CASTEP) [27]. The virtual crystal approximation (VCA) [28] method was used to construct FCC and BCC models of the FeCuMnNi HEA. If the alloying elements are adjacent in the periodic table (i.e., atoms from neighboring rows or columns), the VCA method is typically applicable and effective. The concept of VCA is replacing real alloys with "virtual" metals composed of weighted average values of different alloying elements within the parent alloys. Although VCA is considered a simplified alternative to solid solutions, numerous examples demonstrate the reliability of using VCA for studying alloys composed of refractory elements [29,30]. First, the FCC (BCC) unit cell with a lattice constant of 3.57 Å (2.7 Å) was created and introduced Fe atoms into the cell, containing 4 (2) atoms. Then, we vary the Fe element occupancy concentration within the Fe atoms and incorporate Cu, Mn, and Ni atoms based on their respective concentrations. This method is suitable for alloys with similar chemical elements, and the accuracy has been verified in other work [31,32]. To verify the accuracy of the models, the theoretical X-ray diffraction patterns of the VCA models were computed and compared to experimental results. Reflex achieves the optimal fit between simulated and experimental XRD patterns by optimizing the crystal structure. Simultaneously, it takes into account the crystal's energy to achieve a joint optimization of similarity and potential energy between experimental and simulated, resulting in a crystal structure that not only matches the experimental but is also close to the minimum potential energy. Reflex can dynamically update as the crystal structure changes and can be fine-tuned by incorporating various experimental conditions and correction factors to achieve the best consistency between simulation and experimental data. For more detailed information about Reflex, one can refer to Ref. [33]. The theoretical XRD analysis is based on the Bragg-Brentano diffraction principle, with a scanning angle range of 20° to 90°. The Bragg-Brentano correction was using Eq. (1) [34]:

$$2\theta_{corr} = 2\theta + T_0 + T_1 cos(\theta) + T_2 sin(2\theta) \tag{1}$$

where T_0 is the zero-point correction,

$$T_1 = \left(\frac{180}{\pi}\right)\frac{(t-s)}{R} \tag{2}$$

$$T_2 = \left(\frac{180}{\pi}\right)\frac{1}{2mR} \tag{3}$$

where s is the displacement of the sample surface for the axis of the goniometer, R is the radius of the goniometer circle, and m is the linear absorption coefficient of the sample.

Through the calculation of formation energy, spinodal decomposition energy, and density of states (DOS) for FeCuMnNi HEA, we analyze the factors contributing to its spinodal decomposition. The Perdew-Burke-Ernzerhof (PBE) in the general-gradient-approximation (GGA) function was used to describe the accuracy of the exchange–correlation formalism [35,36]. The relationship between the ion nuclei and valence electrons is represented by the ultra-soft pseudo-potential (USPP) [37]. It's worth noting that USPP is used here because it effectively captures the thermal equilibrium properties of Cu in Fe, which is crucial for simulating and analyzing the modulation decomposition trends in FeCuMnNi HEA. The calculation converges when the total energy was less than 5×10^{-6} eV/Å, the force on each atom was below 0.01 eV/Å, the stress deviation was below 0.02 GPa, and the maximum

displacement of each atom during structure relaxation was under 5×10^{-4} Å. The plane-wave cutoff energy is 500 eV. The k point is set to 11 × 11 × 11 according to the Monkhorst-Pack scheme [38] in the Brillouin zone.

The formation energy can be calculated using Eq. (4),

$$E = E_{total} - xE_{Fe} - yE_{Cu} - nE_{Mn} - mE_{Ni} \quad (4)$$

where, E_{total} is the total energy of FeCuMnNi, E_{Fe}, E_{Cu}, E_{Mn}, and E_{Ni} are the energies of Fe, Cu, Mn, and Ni atoms respectively, and, x, y, n and m refer to the concentration of each element.

The spinodal decomposition energy is calculated using Eq. (5),

$$\Delta E = E_{Solution}^{yCu} - \left(1 - \frac{y}{0.25}\right) E_{Solution}^{0Cu} - \frac{y}{0.25} E_{Solid}^{0.25Cu} \quad (5)$$

where ΔE is the spinodal decomposition energy, $E_{Solution}^{yCu}$ is the total energy of a solid solution containing y concentration Cu, $E_{Solution}^{0Cu}$ is the total energy of solid solution without Cu (i.e. the total energy of FeMnNi), and $E_{Solid}^{0.25Cu}$ is the total energy of a solid solution containing 0.25Cu concentration (i.e. the total energy of FeCuMnNi).

Molecular dynamics simulation

The molecular dynamics simulation of the displacement cascade of the FeCuMnNi HEA and pure Ni is completed by the large-scale atomic/molecular massively parallel simulator (LAMMPS) [39]. First, a pure Fe (Ni) model with a lattice parameter of 3.57 Å (3.52 Å) was created. The Fe atoms in pure Fe are randomly substituted with Cu, Mn, or Ni atoms based on their respective atomic percentages. Then, the initially constructed FeCuMnNi alloy models were simulated with hybrid MC/MD at 300 K to optimize the element distribution. For the hybrid MC/MD simulation, we randomly exchanged the positions of two different types of atoms and calculated the variation in potential energy ΔU before and after the swap. If the energy of the system after the atomic exchange was lower than the energy before, the MC exchange was accepted. Otherwise, there is a probability that it will be accepted according to Eq. (6), and the acceptance criteria for atomic swaps were based on the Metropolis probability value [40].

$$P = e^{\frac{E(i+1)-E(i)}{kT}} \quad (6)$$

where k is the Boltzmann constant and T is the temperature. If a randomly generated number R within the range [0,1] is less than or equal to the Metropolis probability P, then the MC exchange is accepted. Otherwise, the exchange is rejected. In the atom/swap process, the MC steps are interchanged with MD relaxations, and a molecular dynamics calculation is performed for each Monte Carlo exchange, where the energy change before and after the exchange is determined through energy minimization.

The Primary Knock-on Atoms (PKA) with energies of 5 keV, 10 keV, 15 keV, and 20 keV were set in the unit cell, including a $30a \times 30a \times 30a$ unit cell for E_{PKA} of 5 keV, a $40a \times 40a \times 40a$ unit cell for E_{PKA} of 10 keV, a $50a \times 50a \times 50a$ unit cell for E_{PKA} of 15 keV, and a $60a \times 60a \times 60a$ unit cell for E_{PKA} of 20 keV. For convenience, we referred to it as 30 model, 40 model, 50 model, and 60 model, respectively, for short. a is the equilibrium lattice constant. The simulation is divided into two parts in the whole process. A thermostat area is established in the outermost layer of models to ensure that the simulation area maintains a certain temperature. The thickness of the thermostat area depends on the size of the system. The 30 model is 3 lattice units, 40 model is 4 lattice units, 50 model is 5 lattice units, and 60 model is 6 lattice units. The simulation area of the cascade collision is located within models. Before initiating the cascade simulation, the conjugate gradient method [41] was used to minimize the energy of the structure obtained from the hybrid MC/MD simulation, followed by relaxation of 30 ps in an isotherm-isobaric ensemble (NPT) at 300 K. The central Fe atom at the top of the model was chosen as the PKA for the simulation, and the [1 3 5] high-index recoil directions [42] was chosen as the incident direction of the PKA atom to avoid channeling effects. In the displacement-cascade process, all atoms are under the constant volume and energy (micro-canonical ensemble, NVE) ensemble, and the simulation time is 150 ps. Ten cascades were simulated for each unit cell at every energy to obtain an average value.

The embedded atom method (EAM) potential, developed by Bonny et al. [43], was used in this study. The Open Visualization Tool (OVITO) was utilized for the resulting visualization and defect analysis [44–46].

Results

Phase structures

The experimental XRD diffractogram of the FeCuMnNi HEA is shown in Fig. 1, together with the theoretical XRD diffractogram obtained from the first principles. Here the experimental diffraction patterns are used to prove the structure of the FeCuMnNi HEA, while DFT is used as an additional benchmark. First of all, it can be seen from the experimental results that the as-cast structure of the FeCuMnNi HEA is an FCC structure. According to the simulation results, it can be found that the theoretical X-ray diffraction of the FCC FeCuMnNi HEA has a peak distribution match with that of the experiment, while that of the BCC FeCuMnNi HEA is far from the experiment in terms of the positions and numbers of strong peaks. This is because the energy difference between the FCC FeCuMnNi HEA and BCC FeCuMnNi HEA is −0.445 eV, indicating that the FCC structure of the FeCuMnNi HEA is more stable. Therefore, the first-principles calculation results can qualitatively analyze the forming FCC phase of the FeCuMnNi HEA, providing a robust theoretical basis for the experiment. Meanwhile, the experimental results further validate the accuracy of the FeCuMnNi HEA model.

Spinodal decomposition

(1) SEM analysis

From Fig. 1, the separation of the FCC diffraction peaks can be observed, divided into FCC1 + FCC2 structures according to the different lattice constants. This phase separation phenomenon also occurs in AlCoCrFeNi and HfNbTiV alloys, and studies have shown that it is

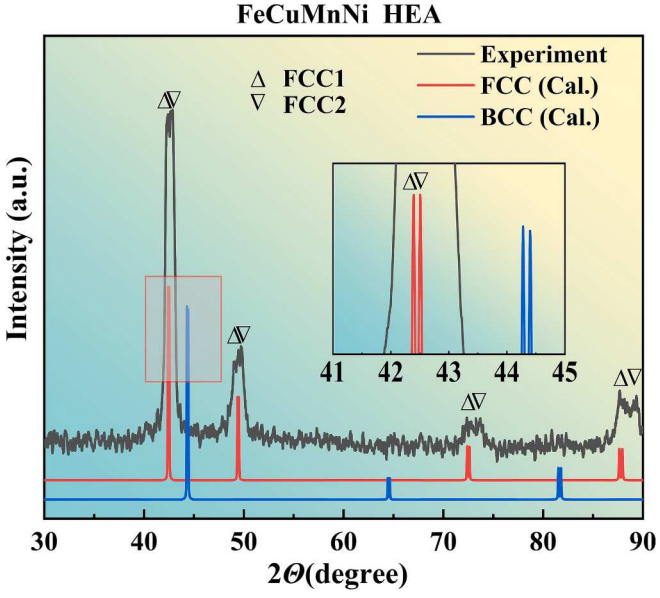

Fig. 1. XRD pattern for the FeCuMnNi HEA.

the result of spinodal decomposition [47,48]. A representative SEM image and its elemental distribution are presented in Fig. 2. The SEM analysis of the FeCuMnNi HEA revealed that the as-cast microstructure is composed of a dendrite-interdendritic phase, where the dendrite (DR) is a Fe-rich region, and the interdendritic (ID) is a Cu-rich area. The distribution of Ni elements is relatively homogeneous throughout the alloy, whereas Mn elements tend to enrich in the interdendritic regions. As exhibited in Table 1, a comparison of the elemental composition between DR and ID reveals significant segregation of components, resulting in different lattice constants between FCC1 and FCC2. The elemental distribution difference in alloys is determined by the nature of each element and the enthalpy of mixing between them. The more negative the enthalpy of mixing between two elements, the stronger the binding force between them. Conversely, the higher the enthalpy of mixing, the more likely they are to separate [49]. The mixing enthalpy, ΔH^{chem}, further shows that Cu exhibits weak binding affinity with Fe, Mn, and Ni due to its high positive mixing enthalpy with other elements. As a result, it is prone to segregation in DR and forms regions rich in Cu. In contrast, Fe-Ni and Mn-Ni exhibit lower mixing enthalpy, resulting in a relatively homogeneous distribution of Ni elements. By comparing the color discrepancy between Mn and Cu in Fig. 2, it is evident that the dendritic region containing Mn appears lighter, indicating its presence within both interdendritic and dendritic regions.

(2) First-principles analysis

The spinodal decomposition of the FeCuMnNi HEA is analyzed via first-principles calculations. The occurrence of phase transition is a result of the thermodynamic instability in the system. The second derivative $(\partial^2 G/\partial c^2)_{T,\ P}$ of the free energy for concentration can be used to verify the stability of a solid solution, where G is the free energy of the alloy and c denotes the concentration of a component. To assess the phase stability of FeCuMnNi HEA, we investigated the thermodynamic and electronic properties of $FeMnNiCu_x$ ($x = 0 \sim 1.1$) HEAs, as presented in Fig. 3. Fig. 3(a) illustrates that the formation energies of $FeMnNiCu_x$ ($x = 0 \sim 1.1$) HEAs become positive with increasing Cu content, while $\partial^2 G/\partial c^2$ is negative. It is concluded from $x = 1$ that the FeMnNiCu HEA is thermodynamically unstable, and the composition fluctuation of Cu will drive the decomposition of the solid solution. FeMnNi is assumed to be the matrix, and $FeMnNiCu_x$ HEAs are regarded as a pseudo-binary alloy to calculate the spinodal decomposition energy of Cu, as illustrated in Fig. 3(a). If the separation energy is positive, the solid-solution phase tends to undergo decomposition, and the trend of decomposition is directly proportional to the separation energy. With the increase in Cu content, the solid solutions will have positive separation energies, indicating that the $FeMnNiCu_x$ HEAs solid solutions within the set composition range have the trend of spinodal decomposition. It can be understood that Cu in the FeMnNiCu HEA readily diffuses and segregates to form Cu-poor and Cu-rich regions. The phase-field method is a viable approach to observing the evolution of the microstructure morphology and spinodal decomposition of the alloy [49–59].

Table 1
Elemental compositions of DR and ID of the cast FeCuMnNi and mixing enthalpy of each element.

Element	ID		DR		ΔH^{chem} (kJ/mol)			
	wt.%	*at.*%	*wt.*%	*at.*%	Fe	Ni	Cu	Mn
Fe	9.32	9.88	44.33	45.43	0	−2	13	0
Ni	19.93	20.09	23.90	23.29	–	0	4	−8
Cu	42.39	39.49	12.96	12.11	–	–	0	4
Mn	28.36	30.55	18.82	19.60	–	–	–	0

To elucidate the electronic origin of the thermodynamic instability, the partial density of states (PDOS) and total density of states (TDOS) of the FeMnNi HEA and FeMnNiCu HEA are calculated, as presented in Fig. 3 (b, c, d, and e). FeMnNi HEA and FeMnNiCu HEA exhibit both spin-up and spin-down DOS. However, the similarity between the spin-up and spin-down DOS in FeMnNi HEA results in weak magnetism, whereas the asymmetric state DOS curves observed in FeMnNiCu HEA indicate strong magnetism. For the FeMnNi HEA, the Fermi level is located in the pseudo gaps of the s, p, and d bands. Consequently, the s, p, and d bands are advantageously filled with electrons in the bonded states (lower energy peaks), while the anti-bonded states (higher energy peaks) are empty. For the FeMnNiCu HEA, although the Fermi level is situated within the pseudo-gap of the s-band, it resides at a higher energy peak in both p- and d-bands. This trend indicates that the electrons in the anti-bonded state occupy the p and d bands. Based on Fig. 3(e), it can be inferred that the d-band mainly contributes to the TDOS of the FeMnNi HEA and FeMnNiCu HEA, and the TDOS of the FeMnNiCu HEA is greater than the FeMnNi HEA after adding Cu. Including electronic states with higher energy in the packed band increases the system energy and makes it thermodynamically unstable [53]. Therefore, it is predicted that the FeMnNiCu HEA will undergo spinodal decomposition after Cu is added through first-principles calculations, and the mechanism is explained.

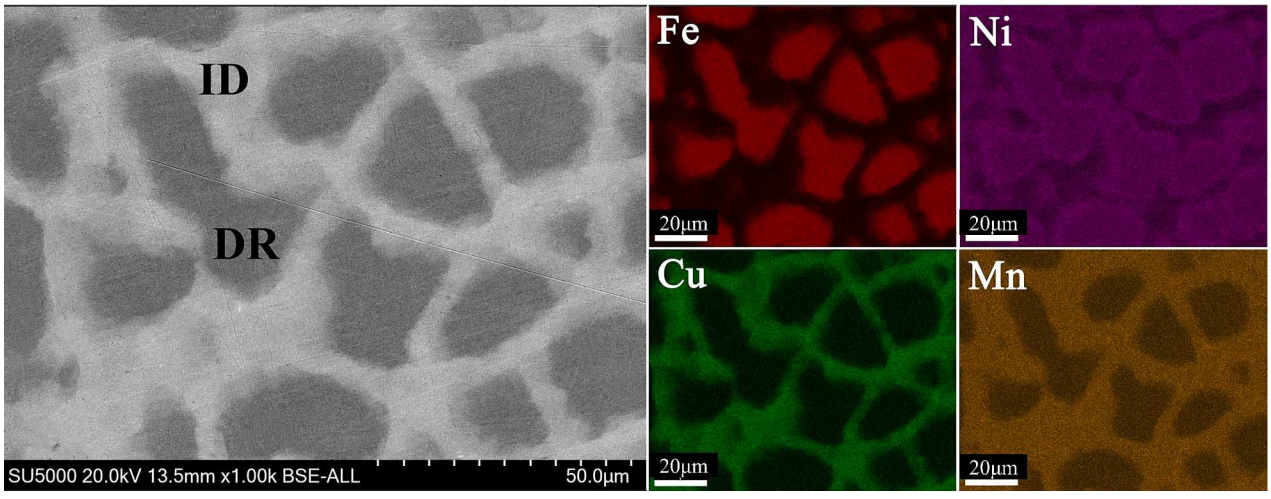

Fig. 2. SEM image of the FeCuMnNi HEA, illustrating the elemental distributions within both dendritic and interdendritic regions. Lighter colors in the distribution of Fe, Ni, Cu, and Mn stand for higher concentrations.

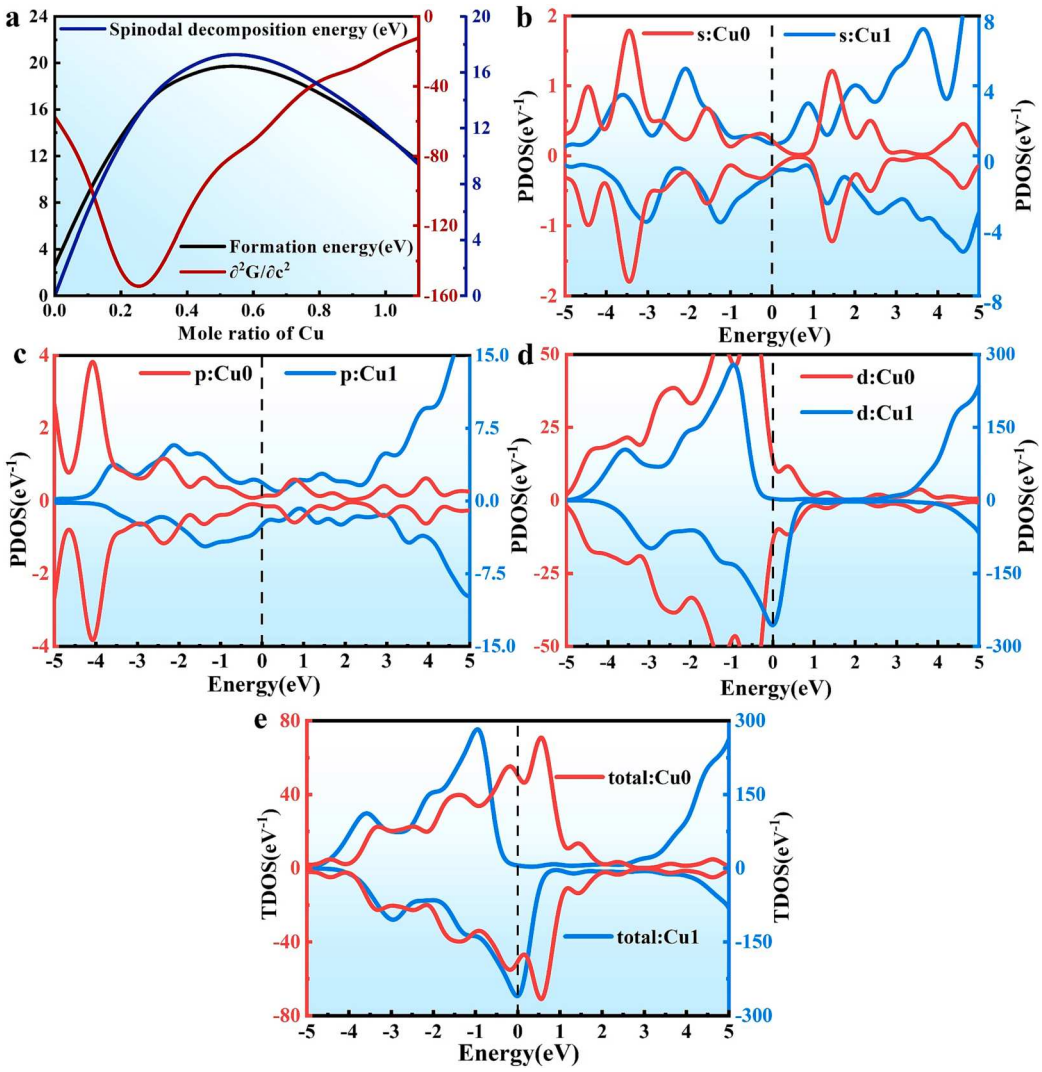

Fig. 3. Thermodynamic and electronic properties of the FeCuMnNi HEA. **a** FeCuMnNi HEA formation energy, the second derivative-function curve of the formation energy with respect to the concentration, and the separation energy of Cu. (**b**, **c**, **d**, and **e**) s-band, p-band, d-band, and total density of states.

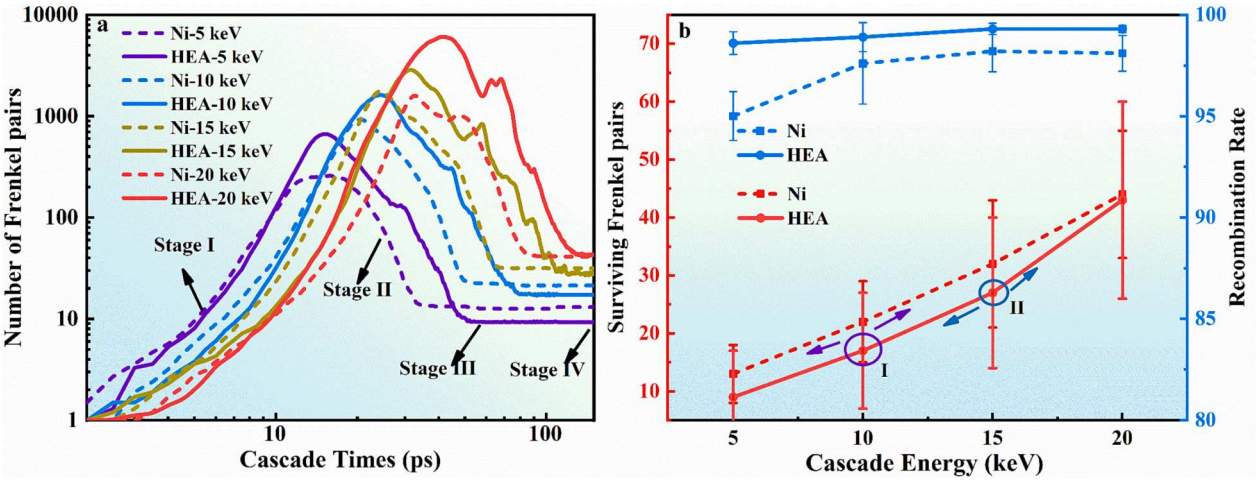

Fig. 4. The number of Frenkel pairs generated by the Ni and FeCuMnNi HEA at different PKA energies (5 keV, 10 keV, 15 keV, and 20 keV). **a** Shows the change curve of the number of Frenkel pairs with the cascade time, **b** Presents the Frenkel pairs that survived the cascade (red curve) and Frenkel-pair recombination rate (blue curve). The numbers shown in the figure are the average values of 10 secondary cascade simulations, with a duration of 150 ps. (For interpretation of the references to color in this figure legend, the reader is referred to the web version of this article.)

Radiation damage

Fig. 4 exhibits the number of Frenkel pairs generated by the FeCuMnNi HEA and pure Ni under different PKA energies. From Fig. 4 (a), it is evident that the irradiation process comprises four distinct stages: collision, thermal-spike, primary damage retention, and thermal defect migration stage. Comparing the defect curve of the FeCuMnNi HEA and Ni under identical PKA energy, it is observed that the collision stage in FeCuMnNi HEA consumes more time, and the defect number generated in the thermal peak stage is higher than the Ni. After the cascade collision, the number of residual Frenkel pairs in the FeCuMnNi HEA is lower than that in the Ni when the PKA energy is at 5 to 15 keV. However, the number of residual Frenkel pairs in the FeCuMnNi HEA is similar to the Ni at 20 keV. Additionally, secondary peaks are observed in the FeCuMnNi HEA due to the formation of defects triggered by elastic waves passing through the unit cell. According to reports, the secondary peak has no impact on the final cascade damage [60].

In the Frenkel-pair quenching stage, interstitial atoms move to the vacancy by diffusion, resulting in a high recombination probability of the vacancy. From Fig. 4(b), it can be observed that the Frenkel-pair recombination rate in FeCuMnNi HEA is higher than that of Ni. This is because the HEAs have certain atomic-level stresses inside the alloy due to the size difference of atoms, which confer excellent self-healing ability upon HEAs [61]. However, the recombination of Frenkel pairs is not solely attributed to this factor, as it is closely intertwined with the diffusion coefficient of interstitial atoms and vacancies [62]. Lin et al. [16] explained the reason why NiCoCrFe HEA has a higher defect recombination rate than pure Ni in terms of thermal peak, thermal conductivity, and interstitial binding energy. Li et al. [63] showed that the vacancy and interstitial atoms of CoNiCrFeMn have similar mobility, which means that the synchronization of interstitial and vacancy migration could increase the probability of recombination. It is evident from Fig. 4(b) that the recombination rate exhibited a significant increase at 10 keV in the Ni, followed by a subsequent tendency to stabilize. For the FeCuMnNi HEA, the recombination rate exhibits a linear growth trend as PKA energy increases. The red curve in Fig. 4(b) presents the residual Frenkel pairs in the FeCuMnNi HEA and Ni at different PKA energies. From position I, it can be found that 10 keV is the inflection point of residual Frenkel pairs changes in the FeCuMnNi HEA, and the number of residual Frenkel pairs increases obviously on the right side of the inflection point. Afterward, the growth trend of the residual Frenkel pairs in Ni remained unchanged, while FeCuMnNi HEA exhibited a second inflection point (position II) at 15 keV.

Fig. 5 shows the evolution of the Frenkel pair at the end of the cascade. When the E_{PKA} is 5 keV, isolated interstitial-atom/vacancies are present in Ni and FeCuMnNi HEA. When the PKA energy is 10 keV, small interstitial clusters are produced in the Ni, and the dumbbell-shaped interstitial atoms (vacancies) defects are formed in the FeCuMnNi HEA. As the PKA energy increases to 15 keV, dumbbell-shaped interstitial-vacancies are formed in the FeCuMnNi HEA. The increase of E_{PKA} accelerates the formation of vacancy clusters [Fig. 5(d) and (h)] and the formation trend of large vacancy clusters is observed. Simultaneously, when the PKA energy is 15 keV, the 1/3<111> Frank dislocation loop, 1/6<110> Stair-rod dislocation loop, and 1/6<112> Shockley dislocation loop appear in the Ni. When the PKA energy is 5 to 15 keV, 1/6<112> Shockley dislocation loops appear in the FeCuMnNi HEA. When the energy increased to 20 keV, mixed dislocations appeared in the FeCuMnNi HEA, including 1/6<112> Shockley dislocation loops and 1/6<110> Stair-rod dislocation loops. Meanwhile, 1/3<110> Hirth dislocation loop appears in Ni. Moreover, it can be seen intuitively from Fig. 5 that the 1/6<112> Shockley dislocation loops in the FeCuMnNi HEA are mainly formed by the aggregation of interstitial atoms, while the aggregation of vacancies mainly forms the 1/6<110> Stair-rod dislocation loops.

The numbers of interstitial atoms distributed in the clusters under different PKA energies are presented in Fig. 6 (a)-(d). For all E_{PKA} considered, the FeCuMnNi HEA has smaller sizes and fewer interstitial clusters than pure Ni, indicating that the kinetics of interstitial clustering is suppressed in the former. However, the inhibitory effect on cluster formation depends on E_{PKA}. When E_{PKA} increases from 5 to 10 keV, FeCuMnNi HEA has more single interstitial-atom defects than Ni after cascade simulations. Nevertheless, the total number of interstitial atoms (or Frenkel pairs) in the FeCuMnNi HEA is slightly smaller than that in the Ni (see Fig. 4), suggesting that the interstitial clusters of the FeCuMnNi HEA may be inhibited. The number of clusters containing 11–30 interstitial atoms increases with the PKA energy in the two materials [Fig. 6(b)]. In connection with Fig. 4(b), it can be considered that 10 keV is the threshold energy to form clusters containing 11–30 interstitial atoms. Ullah et al. [64] mentioned that this inflection point can serve as the threshold energy to form large interstitial clusters (containing 50 or more interstitial groups in pure Ni). When E_{PKA} reaches 20 keV, the number of single interstitial atoms in the Ni increases sharply compared to FeCuMnNi HEA, and there are no clusters containing more than 30 interstitial atoms. For the FeCuMnNi HEA, clusters containing more than 50 interstitial atoms are formed, leading to a reduction in single interstitial and small-sized clusters. In connection

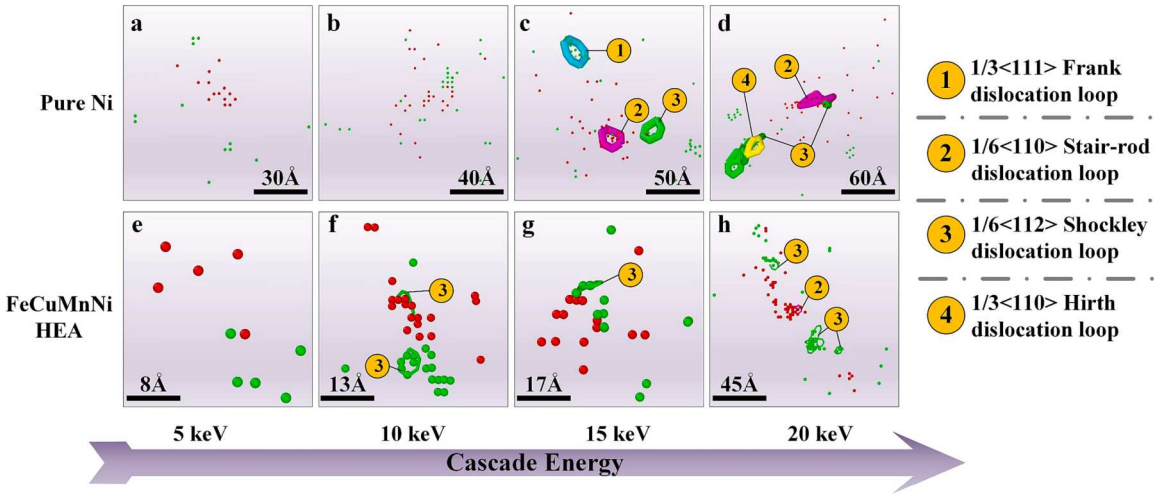

Fig. 5. Frenkel-pairs evolution diagram at the end of the cascade, red represents vacancies, and green represents denotes interstitial-atoms. e, f, g, and h are the amplified images of the FeCuMnNi HEA irradiation region. (For interpretation of the references to color in this figure legend, the reader is referred to the web version of this article.)

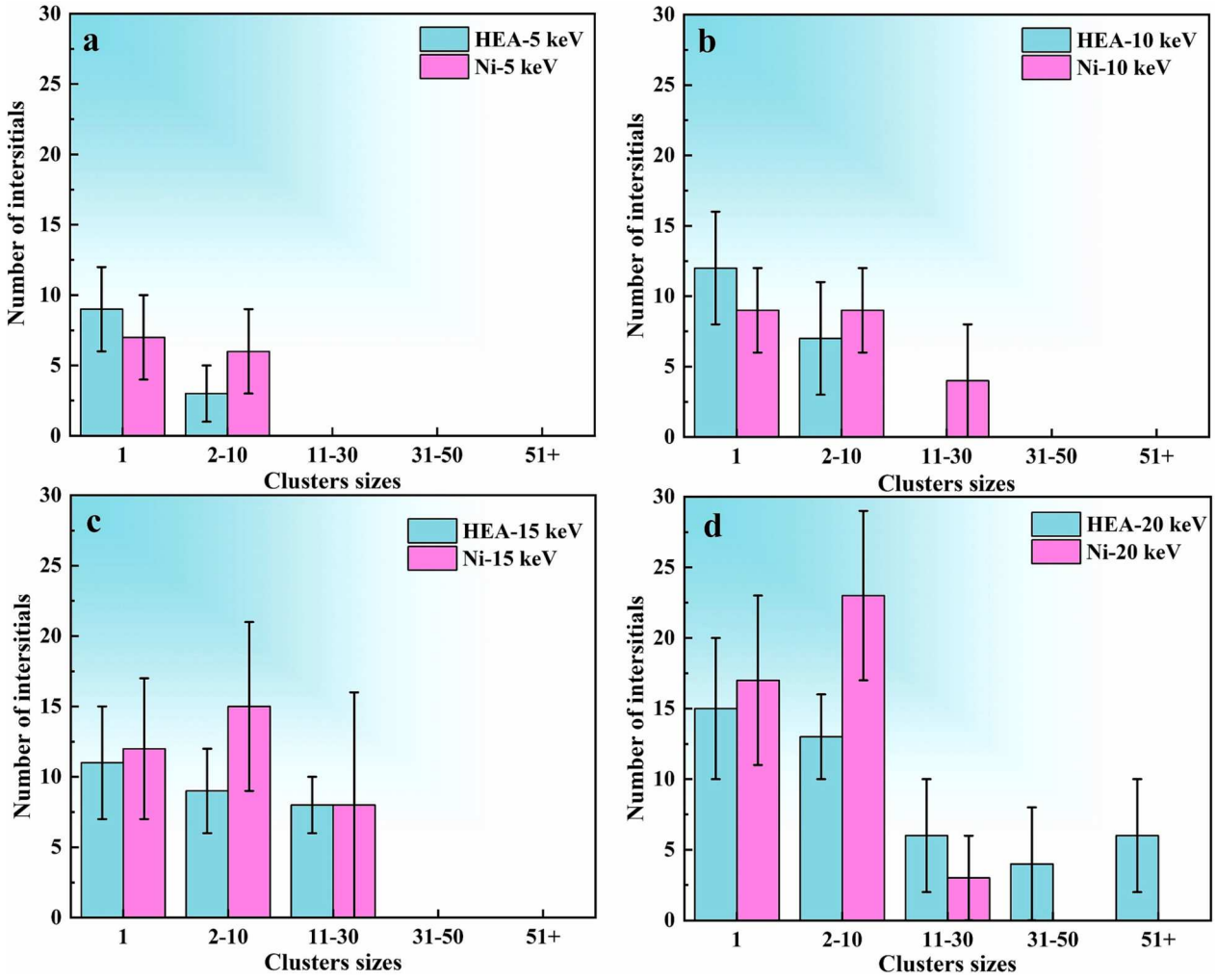

Fig. 6. The number of interstitial atoms contained in clusters of different sizes in the FeCuMnNi HEA and Ni after displacement-cascade simulations. The numbers shown in the figure are the average of 10-cascaded simulations, and the simulation time is 150 ps.

with Fig. 4(b), it can be found that 15 keV is the second inflection point in the FeCuMnNi HEA.

Fig. 7 presents the distribution of vacancy numbers in the clusters under varying E_{PKA}. When E_{PKA} ranges from 5 to 20 keV, Ni has more single vacancy defects than the FeCuMnNi HEA after cascade simulations, while the number of clusters containing 2–10 vacancies is less than that of the FeCuMnNi HEA. However, at 20 keV, the number of clusters containing 11–30 vacancies formed in the FeCuMnNi HEA is more than that in the Ni, nearly 9 % of the vacancies separated to form clusters containing 31–50 vacancies, and nearly 2 % of the vacancies separated to form clusters containing 50 + vacancies. These results indicate that the vacancies in the FeCuMnNi HEA tend to form large-scale clusters under high PKA energies.

Discussion

Method discussion

Although VCA is considered a simplified alternative to solid solutions, the VCA approximation's major limitation lies in its disregard for the atomic local environment, particularly the potential presence of local chemical ordering. Nonetheless, this limitation did not exert a significant impact on our research results. The XRD simulation results of the FeCuMnNi HEA were consistent with experimental results, and the spinodal decomposition energy and DOS accurately described the instability and segregation tendencies of Cu in the FeCuMnNi HEA. Therefore, in this study, the VCA method was applicable.

In addition, although we previously mentioned that USPP effectively captures the thermal equilibrium properties of Cu in Fe, it is worth noting that USPP tends to overestimate the magnetic moments of magnetic materials and cannot correctly describe the strongly varying core part of the valence d-like orbitals [65]. Its accuracy for other properties involving Fe, Ni, and Mn elements is significantly lower compared to PAW. Therefore, when computing relevant properties of magnetic materials, the use of PAW is more accurate.

The molecular dynamics model was constructed according to the experimental results to restore the alloy structure and phase composition in the current state as much as possible. The reliability of the model using Metropolis Monte Carlo largely depends on the accuracy of the interatomic potential used in the simulation, so one should be careful when using it as a benchmark for experiments. In this study, the potential for FeCuMnNi alloy, as fitted by Bonny et al., effectively captures atomic interactions within FeCuMnNi alloy. Utilizing Metropolis Monte Carlo can enable models closer to experimental results, thereby facilitating the study of the radiation resistance properties of FeCuMnNi HEA in its current state.

The formation of segregation and clusters

The segregation tendency of elements after irradiation is further

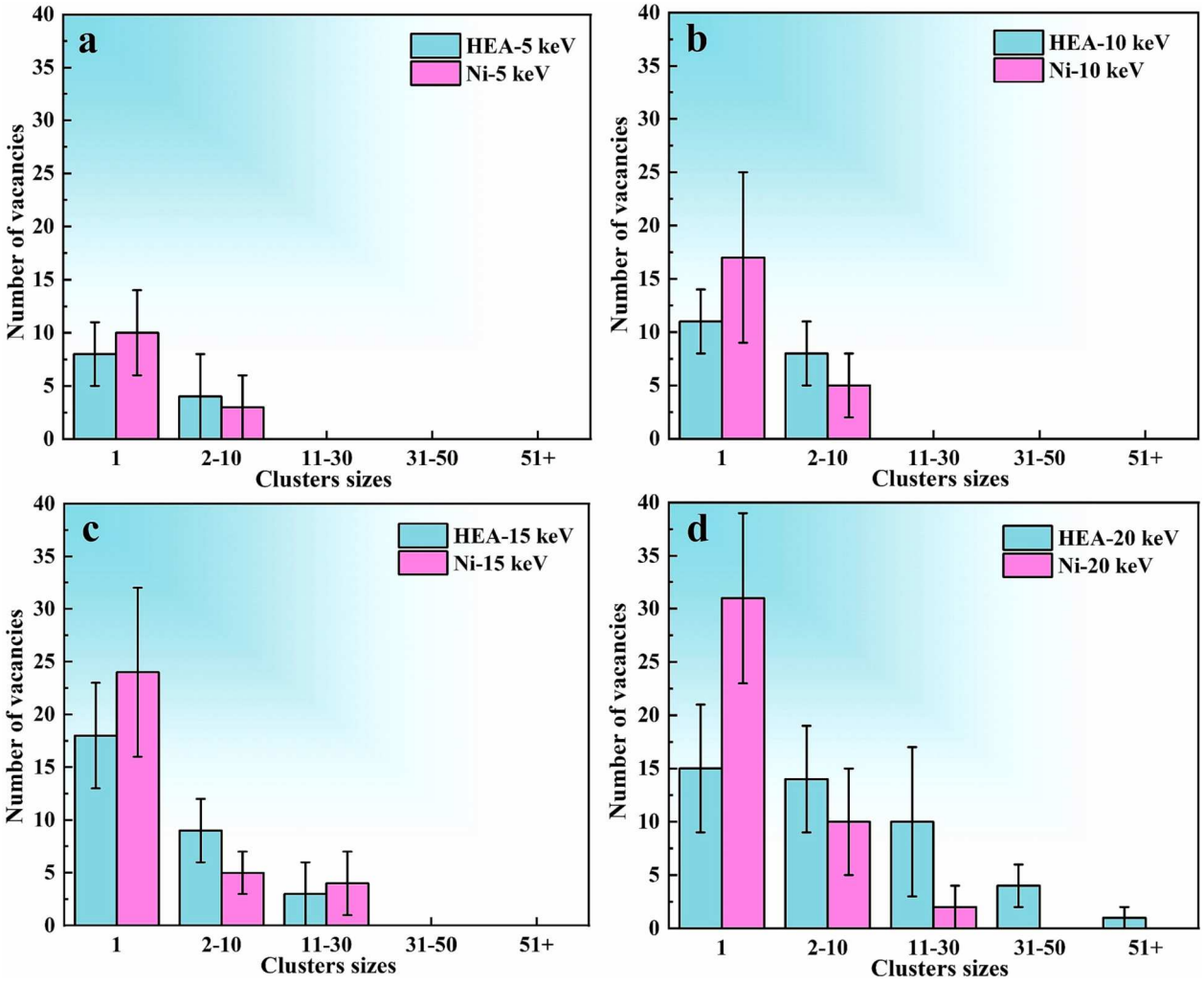

Fig. 7. The number of vacancies contained in clusters of different sizes in the Ni and FeCuMnNi HEA after displacement-cascade simulations. The numbers shown in the figure are the averages of 10-cascaded simulations, and the simulation time is 150 ps.

discussed by correlation function analysis. Take the $60a \times 60a \times 60a$ model as an example, as presented in Fig. 8. The FeCuMnNi HEA still maintains the FCC structure after the hybrid MC/MD simulation and irradiation. After hybrid MC/MD simulations, we observe the strong affinity between Fe-Ni and Mn-Cu pairs from Fig. 8 (a, c, and d), indicating that the FeCuMnNi HEA will form the Fe-Ni-rich and Mn-Cu-rich phases. The strong affinity of Cu-Cu is observed from the first peak in Fig. 8(b), indicating that Cu is easily enriched to form a Cu-rich phase. The hybrid MC/MD simulation result is consistent with the experimental results in Section 3.2, which also proves the validity of our model. Recently, the B2 MnNi ordered phase has been discovered in Chinese commercial SA508Gr.3 steel [66]. In Fig. 8 (c and d), the second peak of Mn-Ni is split into two sub-peaks, and the left shoulder peak indicates the appearance of the short- and medium-range ordered structures [67]. The first principle demonstrates that the B2 MnNi phase has negative formation energy and positive elastic energy modulus, which means that the B2 MnNi phase is a potential precipitated phase in FeCuMnNi HEA. In addition, the content of Cu, Mn, and Ni in FeCuMnNi HEA is significantly higher than that in RPV steel. Therefore, copper may act as a catalyst to promote the formation of the B2 MnNi phase. This is due to the facile formation of Cu-rich precipitates by Cu element in FeCuMnNi high-entropy alloy, which provides a favorable heterophase interface for the nucleation of the B2 MnNi phase [66]. However, further research is necessary to determine whether the ordered phase of FeCuMnNi HEA is the B2 MnNi phase.

After irradiation, the Fe-Ni pair still has a strong affinity, and Cu is still dominated by Cu-rich clusters. Belkacemi et al. [68] have pointed out that under irradiation, the redistribution of Ni atoms occurs through point defect dragging, leading to solute clustering around dislocations, dislocation loops, and vacancies, ultimately triggering the formation of stable phases like Fe_3Ni. In our study, we have overlooked the contribution of point defects to the kinetics of solute cluster formation, and the impact of Ni on the radiation performance of FeCuMnNi HEA is worth investigating. In future work, we will delve into this issue in more detail. It is worth noting that Mn separates from Mn-Cu and begins to form the Mn-Ni-rich phase with Ni, as shown in Fig. 8(h). At the same time, the second peak of Mn-Ni in Fig. 8 (g and h) split into two sub-peaks, and the left shoulder peak indicates the appearance of the short- and medium-range ordered structures. After irradiation, the height of the left shoulder peak is significantly reduced, indicating that the extension of the ordered structure is suppressed. The negative mixing enthalpy between Ni and Mn atoms results in Ni atoms tending to bond with Mn atoms to form Mn-Ni pairs. Therefore, irradiation induces the formation of MnNi clusters. As pointed out by Belkacemi et al. [68], the mechanisms behind solute cluster and phase formation seem to be predominantly radiation-induced rather than radiation-enhanced. Previous studies indicate that the formation of a Mn-Ni-rich phase is considered one of the primary phenomena contributing to irradiation-induced embrittlement and fracture. But we need to further investigate the mechanical properties of irradiated FeCuMnNi HEA, such as tensile and nanoindentation, to

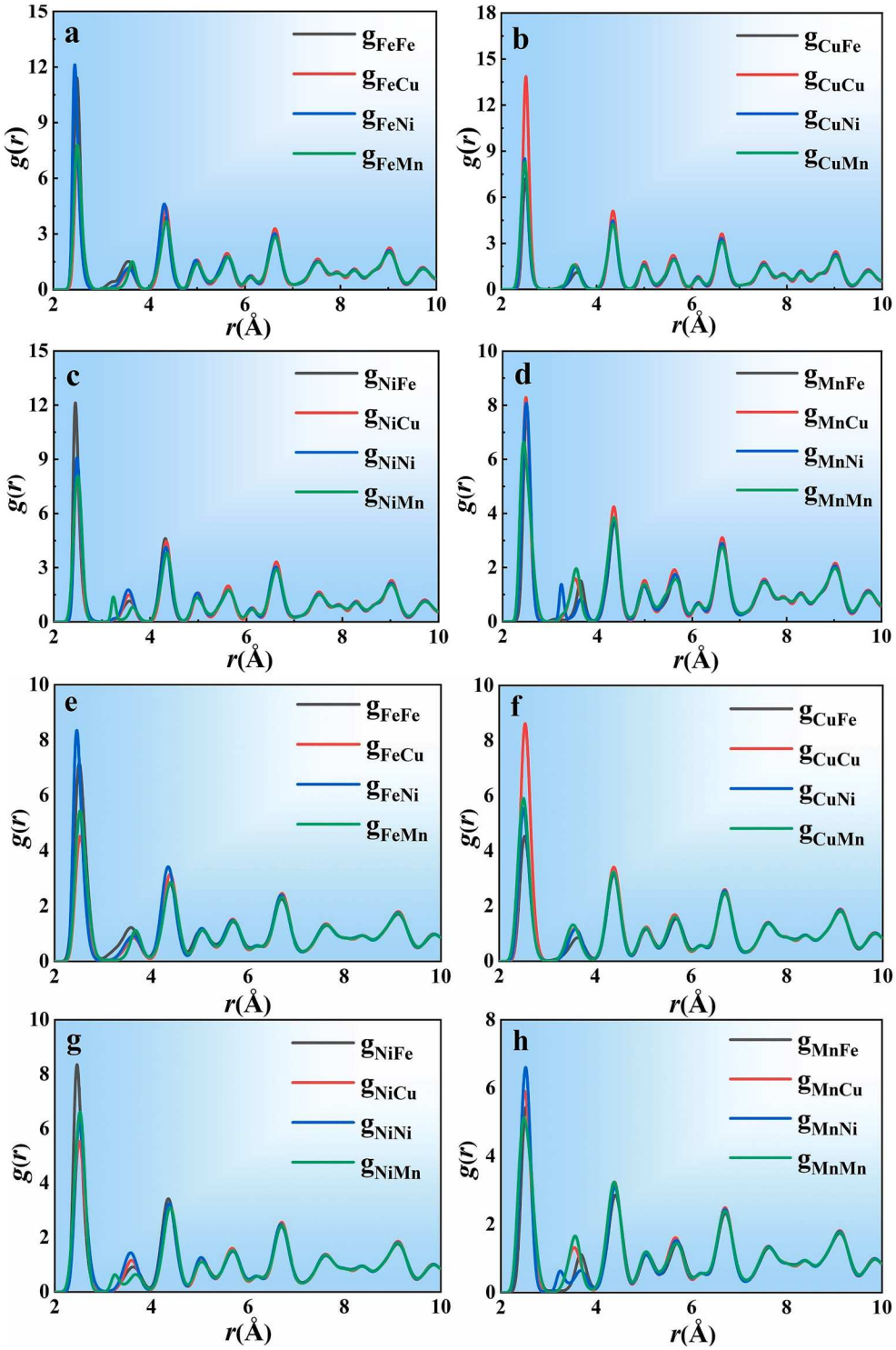

Fig. 8. The pair correlation function of the model after MC simulations (**a**, **b**, **c**, **d**) and after MD displacement cascades (**e**, **f**, **g**, **h**).

assess the influence of Mn-rich phases on the radiation resistance of FeCuMnNi HEA.

The number of defects corresponding to each element explains the reason for the surge of surviving Frenkel pairs in the FeCuMnNi HEA at 20 keV, as shown in Fig. 9. Deluigi et al. [69] discovered that regardless of the type of atoms utilized as PKA, the Cu atoms in the FeNiCrCoCu HEA correspond to the most common defect type. However, in the FeCuMnNi HEA, the most prevalent type of defect observed at E_{PKA} values of 5 or 10 keV is Mn atoms, followed by Cu atoms and Fe atoms the least. Existing research results show that under low-dose irradiation, RPV steels are mainly Cu-rich precipitation, while low-Cu or Cu-free RPV steels will form MnNi-rich precipitation under high-dose irradiation [70,71]. The FeCuMnNi HEA is mainly composed of Cu-Mn clusters and Mn-Ni clusters under low-dose irradiation. When E_{PKA} is 15 keV, the number of Fe atom defects exceeds Cu atoms, forming Fe-Ni clusters [Fig. 9(d)]. However, when E_{PKA} reached 20 keV, the number of Mn atom defects increased sharply, and the FeMnNi large-scale clusters without Cu began to form in the FeCuMnNi HEA. These large-size clusters are the reason for the surge of surviving Frenkel pairs in the FeCuMnNi HEA.

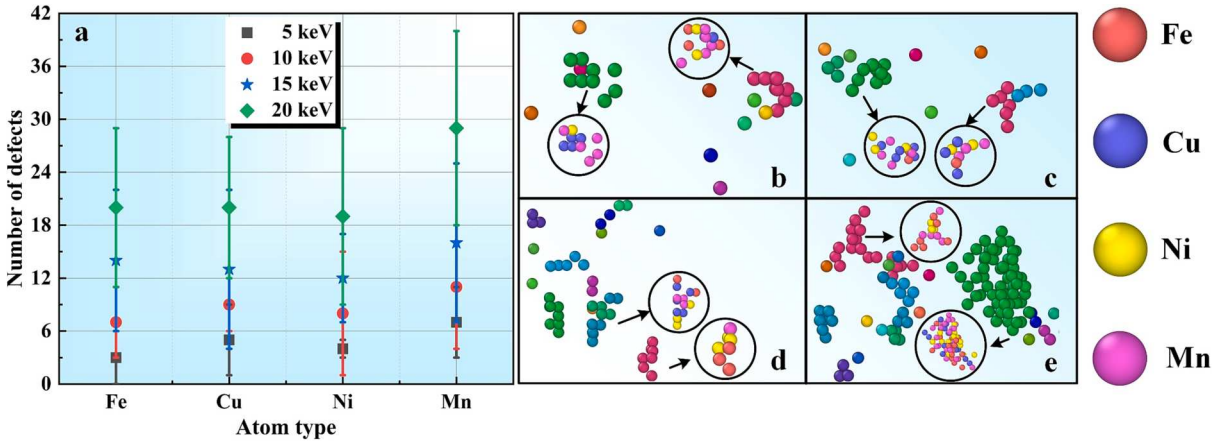

Fig. 9. The number of defects of different atom types (a) and clusters formation at different PKA energies, (b) 5 keV, (c) 10 keV, (d) 15 keV, and (e) 20 keV. The black circles indicate the distribution of different atom types in the corresponding clusters.

Conclusions

In this work, the phase formation of FeCuMnNi HEA was studied through experimental investigations. Furthermore, by combining first-principles calculations, the underlying reasons for the occurrence of spinodal decomposition in FeCuMnNi HEA were elucidated. The irradiation resistance of FeCuMnNi HEA was investigated via molecular dynamics simulations, providing insights into the formation mechanisms of point defects, defect clusters, and dislocation loops. The research results show that:

(1) The FeCuMnNi HEA can undergo spinodal decomposition to form the FCC1 (Fe-rich) + FCC2 (Cu-rich) phases.
(2) The theoretical XRD pattern is in agreement with the experiment. The spinodal decomposition energy and density of states confirm that the instability of Cu in FeCuMnNi HEA alloy leads to its easy segregation.
(3) When the PKA energy is 20 keV, the defect recombination rate after FeMnNiCu HEA irradiation is as high as 99 % compared with Ni (98.1 %). Although FeCuMnNi HEA exhibits better radiation resistance than pure Ni, this does not necessarily imply a direct comparison with RPV steels. Furthermore, BCC alloys are generally more resistant to radiation-induced swelling compared to FCC alloys. Therefore, further research is needed to investigate whether FeCuMnNi HEA has the potential to replace BCC RPV steels in the future.
(4) For the first time, we found that during irradiation, the precipitation phase of the FeCuMnNi HEA is the Mn-rich phase rather than the Cu-rich phase. This unique finding is due to Cu-rich precipitates in the FeCuMnNi HEA providing a favorable heterophase interface for the nucleation of MnNi clusters.

CRediT authorship contribution statement

Qingwei Guo: Conceptualization, Methodology, Software, Validation, Formal analysis, Investigation, Data curation, Writing – original draft, Writing – review & editing. **Jinzhong Tian:** Data curation, Formal analysis. **Xiaotao Xu:** Data curation, Formal analysis. **Hua Hou:** Methodology, Supervision. **Peter K. Liaw:** Writing – review & editing. **Yuhong Zhao:** Supervision, Writing – review & editing.

Declaration of Competing Interest

The authors declare that they have no known competing financial interests or personal relationships that could have appeared to influence the work reported in this paper.

Data availability

Data will be made available on request.

Acknowledgments

National Natural Science Foundation of China (No. 52074246, 52275390, 52205429, 52201146, 52375394), National Defense Basic Scientific Research Program of China (JCKY2020408B002, WDZC2022-12), Key Research and Development Program of Shanxi Province (202102050201011, 202202050201014), Science and Technology Major Project of Shanxi Province (20191102008, 20191102007), Guiding Local Science and Technology Development Projects by the Central Government (YDZJSX2022A025, YDZJSX2021A027) are belonging to the China Fund.National Science Foundation (DMR-1611180 and 1809640) and (2) the Army Research Office (W911NF-13-1-0438 and W911NF-19-2-0049) are belonging to the United States Fund.

References

[1] M. Laver, B.J. Connolly, C. Cooper, J. Kohlbrecher, S. Samothrakitis, K. Wilford, Characterizing accelerated precipitation in proton irradiated steel, J. Nucl. Mater. 557 (2021), 153195, https://doi.org/10.1016/j.jnucmat.2021.153195.
[2] W.K. Yang, X.A. Jiang, X.L. Tian, H.H. Hou, Y.H. Zhao, Phase-field simulation of nano-α' precipitates under irradiation and dislocations, J. Mater. Res. Technol. 22 (2023) 1307–1321, https://doi.org/10.1016/j.jmrt.2022.11.165.
[3] G.R. Odette, T. Yamamoto, T.J. Williams, R.K. Nanstad, C.A. English, On the history and status of reactor pressure vessel steel ductile to brittle transition temperature shift prediction models, J. Nucl. Mater. 526 (2019), 151863, https://doi.org/10.1016/j.jnucmat.2019.151863.
[4] J.J. Shi, W.Z. Zhao, Y.C. Wu, X.B. Liu, J. Jiang, X.Z. Cao, B.Y. Wang, Evolution of microstructures and hardening property of initial irradiated, post-irradiation annealed and re-irradiated Chinese-type low-Cu reactor pressure vessel steel, J. Nucl. Mater. 523 (2019) 333–341, https://doi.org/10.1016/j.jnucmat.2019.06.022.
[5] C.L. Xu, X.B. Liu, Y.F. Li, W.Q. Jia, Q.W. Quan, W.J. Qian, J. Yin, X. Jin, The development of prediction model on irradiation embitterment for low Cu RPV steels, Heliyon 9 (2023) e16581.
[6] K. Murakami, Influence of copper precipitates on clustering behavior of alloying elements observed in Japanese reactor pressure vessel surveillance materials using atom probe tomography, J. Nucl. Mater. 542 (2020), 152508, https://doi.org/10.1016/j.jnucmat.2020.152508.
[7] M.K. Miller, K.F. Russell, Embrittlement of RPV steels: An atom probe tomography perspective, J. Nucl. Mater. 371 (2007) 145–160, https://doi.org/10.1016/j.jnucmat.2007.05.003.
[8] N. Castin, G. Bonny, M.J. Konstantinović, A. Bakaev, F. Bergner, C. Courilleau, C. Domain, B. Gómez-Ferrer, J.M. Hyde, L. Messina, G. Monnet, M.I. Pascuet, B. Radiguet, M. Serrano, L. Malerba, Multiscale modelling in nuclear ferritic steels: From nano-sized defects to embrittlement, Mater. Today Phys. 27 (2022), 100802, https://doi.org/10.1016/j.mtphys.2022.100802.
[9] N. Almirall, P.B. Wells, T. Yamamoto, K. Wilford, T. Williams, N. Riddle, G. R. Odette, Precipitation and hardening in irradiated low alloy steels with a wide

range of Ni and Mn compositions, Acta Mater. 179 (2019) 119–128, https://doi.org/10.1016/j.actamat.2019.08.027.
[10] J.W. Yeh, S.K. Chen, J.Y. Gan, S.J. Lin, T.S. Chin, T.T. Shun, C.H. Tsau, S.Y. Chang, Formation of simple crystal structures in Cu-Co-Ni-Cr-Al-Fe-Ti-V alloys with multiprincipal metallic elements, Metall. Mater. Trans. A 35 (2004) 2533–2536, https://doi.org/10.1007/s11661-006-0234-4.
[11] B. Cantor, I.T.H. Chang, P. Knight, A.J.B. Vincent, Microstructural development in equiatomic multicomponent alloys, Mat. Sci. Eng. A 375–377 (2004) 213–218, https://doi.org/10.1016/j.msea.2003.10.257.
[12] M.H. Chuang, M.H. Tsai, W.R. Wang, S.J. Lin, J.W. Yeh, Microstructure and wear behavior of $Al_xCo_{1.5}CrFeNi_{1.5}Ti_y$ high-entropy alloys, Acta Mater. 59 (2011) 6308–6317, https://doi.org/10.1016/j.actamat.2011.06.041.
[13] P.J. Shi, R.G. Li, Y. Li, Y.B. Wen, Y.B. Zhong, W.L. Ren, Z. Shen, T.X. Zheng, J.C. PENG, X. Liang, P.F. Hu, N. Min, Y. Zhang, Y. Ren, P.K. Liaw, D. Raabe, Y.D. Wang,, Hierarchical crack buffering triples ductility in eutectic herringbone high-entropy alloys, Science 373 (2021) 912–918, https://doi.org/10.1126/science.abf6986.
[14] X.T. Xu, Y.H. Zhao, H.Q. Li, X.B. Zhang, Y. Pan, S. Wang, H. Hou, Enhanced strength in Co-free $Ni_{47.5-x}Fe_{25}Cr_{25}Al_xTi_{2.5}$ high entropy alloys via introducing dual precipitates, J. Mater. Res. Technol. 25 (2023) 5663–5673, https://doi.org/10.1016/j.jmrt.2023.06.266.
[15] R. Feng, Y. Rao, C.H. Liu, X. Xie, D.J. Yu, Y. Chen, M. Ghazisaeidi, T. Ungar, H. M. Wang, K. An, P.K. Liaw, Enhancing fatigue life by ductile-transformable multicomponent B2 precipitates in a high-entropy alloy, Nat. Commun. 12 (2021) 3588, https://doi.org/10.1038/s41467-021-23689-6.
[16] Y.P. Lin, T.F. Yang, L. Lang, C. Shan, H.Q. Deng, W.Y. Hu, F. Gao, Enhanced radiation tolerance of the Ni-Co-Cr-Fe high-entropy alloy as revealed from primary damage, Acta Mater. 196 (2020) 133–143, https://doi.org/10.1016/j.actamat.2020.06.027.
[17] H.S. Do, B.J. Lee, Origin of radiation resistance in multi-principal element alloys, Sci. Rep. 8 (2018) 16015, https://doi.org/10.1038/s41598-018-34486-5.
[18] S.Q. Xia, X. Yang, T.F. Yang, S. Liu, Y. Zhang, Irradiation resistance in $Al_xCoCrFeNi$ high entropy alloys, JOM 67 (2015) 2340–2344, https://doi.org/10.1007/s11837-015-1568-4.
[19] Q. Xu, H.Q. Guan, Z.H. Zhong, S.S. Huang, J.J. Zhao, Irradiation resistance mechanism of the CoCrFeMnNi equiatomic high-entropy alloy, Sci. Rep. 11 (2021) 608, https://doi.org/10.1038/s41598-020-79775-0.
[20] S. Zhang, K. Nordlund, F. Djurabekova, F. Granberg, Y. Zhang, T.S. Wang, Radiation damage buildup by athermal defect reactions in nickel and concentrated nickel alloys, Mater. Res. Lett. 5 (2017) 433–439, https://doi.org/10.1080/21663831.2017.1311284.
[21] C.Y. Lu, L.L. Niu, N.J. Chen, K. Jin, T.N. Yang, P.Y. Xiu, Y.W. Zhang, F. Gao, H. B. Bei, S. Shi, M.R. He, I.M. Robertson, W.J. Weber, L.M. Wang, Enhancing radiation tolerance by controlling defect mobility and migration pathways in multicomponent single-phase alloys, Nat. Commun. 7 (2016) 13564, https://doi.org/10.1038/ncomms13564.
[22] G. Velişa, M.W. Ullah, H.Z. Xue, K. Jin, M.L. Crespillo, H.B. Bei, W.J. Weber, Y. W. Zhang, Irradiation-induced damage evolution in concentrated Ni-based alloys, Acta Mater. 135 (2017) 54–60, https://doi.org/10.1016/j.actamat.2017.06.002.
[23] C.Y. Lu, T.N. Yang, K. Jin, N. Gao, P.Y. Xiu, Y.W. Zhang, F. Gao, H.B. Bei, W. J. Weber, K. Sun, Y. Dong, L.M. Wang, Radiation-induced segregation on defect clusters in single-phase concentrated solid-solution alloys, Acta Mater. 127 (2017) 98–107, https://doi.org/10.1016/j.actamat.2017.01.019.
[24] S.M. Chen, Z.J. Ma, S. Qiu, L.J. Zhang, S.Z. Zhang, R. Yang, Q.M. Hu, Phase decomposition and strengthening in HfNbTaTiZr high entropy alloy from first-principles calculations, Acta Mater. 225 (2022), 117582, https://doi.org/10.1016/j.actamat.2021.117582.
[25] G.J. Ge, F.D. Chen, X.B. Tang, H. Huang, J.W. Lin, S.K. Shen, J. Gao, Effects of interstitial carbon on the radiation tolerance of carbon-doped NiFe binary alloys from atomistic simulations, Nucl. Mater. Energy 24 (2020), 100785, https://doi.org/10.1016/j.nme.2020.100785.
[26] F.J.J. Leusen, S. Wilke, P. Verwer, G.E. Engel, Computational approaches to crystal structure and polymorph prediction, Implications of Molecular and Materials Structure for New Technologies, NATO Science Series, vol. 360 (1999) Springer, Dordrecht. Doi: 10.1007/978-94-011-4653-1_22.
[27] S.J. Clark, M.D. Segall, C.J. Pickard, P.J. Hasnip, M.J. Probert, K. Refson, M. C. Payne, First principles methods using CASTEP, Z. Kristallogr. 220 (2005) 567–570, https://doi.org/10.1524/zkri.220.5.567.65075.
[28] L. Bellaiche, D. Vanderbilt, Virtual crystal approximation revisited: Application to dielectric and piezoelectric properties of perovskites, Phys. Rev. B 61 (2000) 7877–7882, https://doi.org/10.1103/PhysRevB.61.7877.
[29] T.S. Li, J.W. Morris Jr., N. Nagasako, S. Kuramoto, D.C. Chrzan, "Ideal" engineering alloys, Phys. Rev. Lett. 98 (2007), 105503, https://doi.org/10.1103/PhysRevLett.98.105503.
[30] L. Qi, D.C. Chrzan, Tuning ideal tensile strengths and intrinsic ductility of bcc refractory alloys, Phys. Rev. Lett. 112 (2014), 115503, https://doi.org/10.1103/PhysRevLett.112.115503.
[31] S. Wang, J. Xiong, D. Li, Q. Zeng, M. Xiong, X.S. Chai, Comparison of two calculation models for high entropy alloys: Virtual crystal approximation and special quasi-random structure, Mater. Lett. 282 (2021), 128754, https://doi.org/10.1016/j.matlet.2020.128754.
[32] M.X. Wang, H. Zhu, G.J. Yang, J.F. Li, L.T. Kong, A generally reliable model for composition-dependent lattice constants of substitutional solid solutions, Acta Mater. 211 (2021), 116865, https://doi.org/10.1016/j.actamat.2021.116865.
[33] https://www.addlink.es/images/pdf/agdweb930.pdf.
[34] A.J.C. Wilson, Mathematical theory of X-ray powder diffraction, Philips Technical Library, Eindhoven, 1963.
[35] J.P. Perdew, K. Burke, M. Ernzerhof, Generalized gradient approximation made simple, Phys. Rev. Lett. 77 (1996) 3865–3868, https://doi.org/10.1103/PhysRevLett.77.3865.
[36] Y.H. Zhao, S. Wang, B. Zhang, Y. Yuan, Q.W. Guo, H. Hou, The anisotropy of three-component medium entropy alloys in AlCoCrFeNi system: First-principle studies, J. Solid State Chem. 276 (2019) 232–237, https://doi.org/10.1016/j.jssc.2019.05.003.
[37] D. Vanderbilt, Soft self-consistent pseudopotentials in a generalized eigenvalue formalism, Phys. Rev. B 41 (1990) 7892–7895, https://doi.org/10.1103/PhysRevB.41.7892.
[38] H.J. Monkhorst, J.D. Pack, Special points for Brillouin-zone integrations, Phys. Rev. B 13 (1976) 5188–5192, https://doi.org/10.1103/PhysRevB.13.5188.
[39] S. Plimpton, Fast parallel algorithms for short-range molecular dynamics, J. Comput. Phys. 117 (1995) 1–19, https://doi.org/10.1006/jcph.1995.1039.
[40] N. Metropolis, A.W. Rosenbluth, M.N. Rosenbluth, A.H. Teller, E. Teller, Equation of state calculations by fast computing machines, J. Chem. Phys. 21 (1953) 1087–1092.
[41] M.R. Hestenes, E. Stiefel, Methods of conjugate gradients for solving linear systems, J. Res. Nat. Bur. Stand. 49 (1952) 2379.
[42] F. Gao, D. Chen, W.Y. Hu, W.J. Weber, Energy dissipation and defect generation in nanocrystalline silicon carbide, Phys. Rev. B 81 (2010), 184101, https://doi.org/10.1103/PhysRevB.81.184101.
[43] G. Bonny, D. Terentyev, A. Bakaev, E.E. Zhurkin, M. Hou, D.V. Neck, L. Malerba, On the thermal stability of late blooming phases in reactor pressure vessel steels: an atomistic study, J. Nucl. Mater. 442 (2013) 282–291, https://doi.org/10.1016/j.jnucmat.2013.08.018.
[44] A. Stukowski, Structure identification methods for atomistic simulations of crystalline materials, Modelling Simul. Mater. Sci. Eng. 20 (2012), 045021, https://doi.org/10.1088/0965-0393/20/4/045021.
[45] Q.W. Guo, H. Hou, Y. Pan, X.L. Pei, Z. Song, P.K. Liaw, Y.H. Zhao, Hardening-softening of $Al_{0.3}CoCrFeNi$ high-entropy alloy under nanoindentation, Mater. Design 231 (2023), 112050.
[46] Q.W. Guo, H. Hou, K.L. Wang, M.X. Li, P.K. Liaw, Y.H. Zhao, Coalescence of $Al_{0.3}CoCrFeNi$ polycrystalline high-entropy alloy in hot-pressed sintering: a molecular dynamics and phase-field study, NPJ Comput. Mater. 9 (2023) 185, https://doi.org/10.1038/s41524-023-01139-9.
[47] W.R. Wang, W.L. Wang, S.C. Wang, Y.C. Tsai, C.H. Lai, J.W. Yeh, Effects of Al addition on the microstructure and mechanical property of $Al_xCoCrFeNi$ high-entropy alloys, Intermetallics 26 (2012) 44–51, https://doi.org/10.1016/j.intermet.2012.03.005.
[48] Z.B. An, S.C. Mao, T. Yang, C.T. Liu, B. Zhang, E. Ma, H. Zhou, Z. Zhang, L.H. W, X. D. Han, Spinodal-modulated solid solution delivers a strong and ductile refractory high-entropy alloy, Mater. Horiz. 8 (2021) 948–955, https://doi.org/10.1039/D0MH01341B.
[49] P. Cheng, Y.H. Zhao, X.T. Xu, S. Wang, Y.Y. Sun, H. Hou, Microstructural evolution and mechanical properties of $Al_{0.3}CoCrFeNiSi_x$ high-entropy alloys containing coherent nanometer-scaled precipitates, Mat. Sci. Eng. A 772 (2020), 138681, https://doi.org/10.1016/j.msea.2019.138681.
[50] L.Q. Chen, Y.H. Zhao, From classical thermodynamics to phase-field method, Prog. Mater Sci. 124 (2022), 100868, https://doi.org/10.1016/j.pmatsci.2021.100868.
[51] Y.Y. Sun, Y.H. Zhao, B.J. Zhao, Z. Guo, X.L. Tian, W.K. Yang, H. Hou, Multi-component phase-field simulation of microstructural evolution and elemental distribution in Fe-Cu-Mn-Ni-Al alloy, Calphad 69 (2020), 101759, https://doi.org/10.1016/j.calphad.2020.101759.
[52] Y.Y. Sun, Y.H. Zhao, B.J. Zhao, W.K. Yang, X.L. Li, H. Hou, Phase-field modeling of microstructure evolution of Cu-rich phase in Fe-Cu-Mn-Ni-Al quinary system coupled with thermodynamic databases, J. Mater. Sci. 54 (2019) 11263–11278, https://doi.org/10.1007/s10853-019-03678-3.
[53] T.Z. Xin, Y.H. Zhao, R. Mahjoub, J.X. Jiang, A. Yadav, K. Nomoto, R.M. Niu, S. Tang, F. Ji, Z. Quadir, D. Miskovic, J. Daniels, W.Q. Xu, X.Z. Liao, L.Q. Chen, K. Hagihara, X.Y. Li, S. Ringer, M. Ferry, Ultrahigh specific strength in a magnesium alloy strengthened by spinodal decomposition, Sci. Adv. 7 (2021) eabf3039, https://doi.org/10.1126/sciadv.abf3039.
[54] Y.H. Zhao, Understanding and design of metallic alloys guided by phase-field simulations, npj Comput, Mater. 9 (2023) 94, https://doi.org/10.1038/s41524-023-01038-z.
[55] T. Xin, S. Tang, F. Ji, L. Cui, B. He, X. Lin, X. Tian, H. Hou, Y.H. Zhao, M. Ferry, Phase transformations in an ultralight BCC Mg alloy during anisothermal aging, Acta Mater. 239 (2022), 118248, https://doi.org/10.1016/j.actamat.2022.118248.
[56] Y.H. Zhao, H. Xing, L.J. Zhang, H.B. Huang, D.K. Sun, X.L. Dong, Y.X. Sh, J.C. Wang, Development of Phase-Field Modeling in Materials Science in China: A Review, Acta Metall. Sin. (Engl. Lett.) **428** (2023). Doi: 10.1007/s40195-023-01593-w.
[57] Y.H. Zhao, Co-precipitated Ni/Mn shell coated nano Cu-rich core structure: A phase-field study, J. Mater. Res. Technol. 21 (2022) 546–560, https://doi.org/10.1016/j.jmrt.2022.09.032.
[58] Y.H. Zhao, B. Zhang, H. Hou, W. Chen, M. Wang, Phase-field simulation for the evolution of solid/liquid interface front in directional solidification process, J/ Mater. Sci. Technol. 35 (2019) 1052, https://doi.org/10.1016/j.jmst.2018.12.009.
[59] J.B. Zhang, H.F. Wang, W.W. Kuang, Y.C. Zhang, S. Li, Y.H. Zhao, D.M. Herlach, Rapid solidification of non-stoichiometric intermetallic compounds: Modeling and experimental verification, Acta Mater. 148 (2018) 86–99, https://doi.org/10.1016/j.actamat.2018.01.040.

[60] M. Tikhonchev, V. Svetukhin, A. Kadochkin, E. Gaganidze, MD simulation of atomic displacement cascades in Fe-10 at.%Cr binary alloy, J. Nucl. Mater. 395 (2009) 50–57, https://doi.org/10.1016/j.jnucmat.2009.09.015.
[61] T. Egami, W. Guo, P.D. Rack, T. Nagase, Irradiation resistance of multicomponent alloys, Metall. Mater. Trans. A 45 (2014) 180–183, https://doi.org/10.1007/s11661-013-1994-2.
[62] G.S. Was, Fundamentals of radiation materials science: metals and alloys, Second ed., SpringerNature, Springer-Verlag GmbH Berlin Heidelberg, 2016.
[63] Y.G. Li, R. Li, Q. Peng, S. Ogata, Reduction of dislocation, mean free path, and migration barriers by high entropy alloy: insights from the atomistic study of irradiation damage of CoNiCrFeMn, Nanotechnology 31 (2020), 425701, https://doi.org/10.1088/1361-6528/ab9cf5.
[64] M.W. Ullah, D.S. Aidhy, Y.W. Zhang, W.J. Weber, Damage accumulation in ion-irradiated Ni-based concentrated solid-solution alloys, Acta Mater. 109 (2016) 17–22, https://doi.org/10.1016/j.actamat.2016.02.048.
[65] P. Olsson, T.P.C. Klaver, C. Domain, Ab initio study of solute transition-metal interactions with point defects in bcc Fe, Phys. Rev. B 81 (2010), 054102, https://doi.org/10.1103/PhysRevB.81.054102.
[66] H.L. Liu, Q.L. Li, The characterization of a nanoscale MnNi cluster in thermally aged reactor pressure vessel steels, Mater. Res. Express 9 (2022), 026531, https://doi.org/10.1088/2053-1591/ac5550.
[67] K. Zhang, H. Li, L. Li, X.F. Bian, Why does the second peak of pair correlation functions split in quasi-two-dimensional disordered films? Appl. Phys. Lett. 102 (2013), 071907 https://doi.org/10.1063/1.4793187.
[68] L.T. Belkacemi, E. Meslin, B. Décamps, B. Radiguet, J. Henry, Radiation-induced bcc-fcc phase transformation in a Fe-3%Ni alloy, Acta Mater. 161 (2018) 61–72, https://doi.org/10.1016/j.actamat.2018.08.031.
[69] O.R. Deluigi, R.C. Pasianot, F.J. Valencia, A. Caro, D. Farkas, E.M. Bringa, Simulations of primary damage in a high entropy alloy: Probing enhanced radiation resistance, Acta Mater. 213 (2021), 116951, https://doi.org/10.1016/j.actamat.2021.116951.
[70] R. Ngayam-Happy, C.S. Becquart, C. Domain, L. Malerba, Formation and evolution of MnNi clusters in neutron irradiated dilute Fe alloys modelled by a first principle-based AKMC method, J. Nucl. Mater. 426 (2012) 198–207, https://doi.org/10.1016/j.jnucmat.2012.03.033.
[71] P.D. Styman, J.M. Hyde, K. Wilford, A. Morley, G.D.W. Smith, Precipitation in long term thermally aged high copper, high nickel model RPV steel welds, Prog. Nucl. Energy 57 (2012) 86–92, https://doi.org/10.1016/j.pnucene.2011.10.010.